Ultrafast Microscopy of a Twisted Plasmonic Spin Skyrmion

Yanan Dai[a1], Zhikang Zhou[a], Atreyie Ghosh[a], Karan Kapoor[a], Maciej Dąbrowski[b], Atsushi Kubo[c], Chen-Bin Huang[d], and Hrvoje Petek[a2]

[a]Department of Physics and Astronomy, University of Pittsburgh, Pittsburgh, PA 15260, USA

[b]Department of Physics and Astronomy, University of Exeter, Exeter EX4 4QL, United Kingdom

[c]Division of Physics, Faculty of Pure and Applied Sciences, University of Tsukuba, 1-1-1 Tenno-dai, Tsukuba-shi, Ibaraki, 305-8571 Japan

[d]Institute of Photonics Technologies, National Tsing Hua University, Hsinchu 30013, Taiwan

[1,2]To whom the correspondence may be addressed: yad17@pitt.edu, petek@pitt.edu

Abstract: We report a transient plasmonic spin skyrmion topological quasiparticle within surface plasmon polariton (SPP) vortices that is described by analytical modeling and imaging of their formation by ultrafast interferometric time-resolved photoemission electron microscopy (ITR-PEEM). Our model finds a twisted skyrmion spin texture on the vacuum side of a metal/vacuum interface, and its integral opposite counterpart in the metal side. The skyrmion pair forming a hedgehog texture, is associated with co-gyrating anti-parallel electric and magnetic fields, which form intense pseudoscalar $E \cdot B$ focus that breaks the local time-reversal symmetry and can drive magnetoelectric responses of interest to the axion physics. Through nonlinear two-photon photoemission (2PP), we record attosecond precision images of the plasmonic vectorial vortex field evolution with nanometer spatial and femtosecond temporal (nanofemto) resolution, from which we derive the twisted plasmonic spin skyrmion topological textures, their boundary and topological charges; the modeling and experimental measurements establish a quantized integer photonic topological charge that is stable over the optical generation pulse envelope.

Significance statement

Topology engages ideas within solid state materials spanning the nanometer to cosmic scales from subatomic particles to cosmology. Topology can be intrinsic to the lattice and consequent electronic structure, or be imposed on them by intense electromagnetic fields. Skyrmions are known as stable magnetic quasiparticles of interest to fundamental physics, and with potential applications to magnetic data storage and quantum computing. Research on the photonic and plasmonic skyrmions, however, is at its infancy. We present the first ultrafast microscopy imaging study of a plasmonic spin skyrmion generated by the spin-orbit interaction of light. We reveal by experiment and theory the nanofemto plasmonic vortex fields and their topological skyrmion spin textures that can dress topologically trivial materials, drive magnetoelectric phenomena, and probe axion physics.

Keywords
Plasmonic skyrmion, topological plasmonics, ultrafast microscopy, spin-orbit interaction of light, vectorial nonlinear optics, magnetoelectric effect, axion field

I. Introduction

Topological solitons are singular field distributions broadly relevant to the physics and chemistry of structure formation, charge-parity violation, phase transitions relevant to cosmological evolution, nucleons, and condensed matter.[1-7] Skyrmion solitons were first proposed as homotopically nontrivial differential vector field theoretic descriptors of the structure of nucleons,[8] and later were discovered in condensed mater contexts as more accessible homotopes, such as stable field and spin textures in chiral magnets,[9,10] Bose-Einstein condensates,[11,12] liquid crystals,[13] free space vectorial optical fields,[14-17] and plasmon[7,18,19] as well as phonon polaritonic fields.[20]

The discovered plasmonic *field* skyrmion textures form with locally linearly polarized SPP standing wave electric fields oscillating at PHz frequency,[18] such that their topological textures average to zero within each optical cycle and they do not possess a chiral character.[19] Photonic spin angular momentum (SAM), which defines the chiral quantum interactions of light with matter, can also be engineered to possess

skyrmion textures,[7,21] whose topological properties, however, are expected to be stable over the light pulse duration, as has been demonstrated in the half-skyrmion (meron) textures.[22,23] Such topological spin textures, which have escaped scrutiny until methods that can probe them on a deep subwavelength scale had been developed, are formed within plasmonic vortices carrying orbital angular momentum (OAM), despite that structured OAM light has been known for more than 30 years.[6]

Unlike ground state skyrmions, such as those in magnetic materials that form through spin-spin interactions on picosecond time scales,[24] plasmonic spin skyrmions exist and can be investigated in ultrafast *dynamical* contexts where they can impress their properties on matter. When they are created and persist on few femtosecond, or longer timescales of the generating pulse duration, such topological fields can perform Poincaré engineering of matter by impressing their topological field and spin textures on proximate materials in their near field;[25,26] for example, they can induce, topological phase transitions,[10,22,24] nonreciprocal magnetoelectric responses,[27,28] and valley selective interactions in 2D semiconductors.[29-32] They can also control topological quasiparticle functions in trivial materials,[26,33,34] and expand repertoires of optoelectronics, single molecule spectroscopy,[35-37] and topological photonics.[38-40]

Quantitative experimental information on the plasmonic spin skyrmion nanoscale textures, their skyrmion boundaries and integer topological charges, however, are yet to be obtained because of the challenge in the imaging of the nanofemto SPP fields. Moreover, demonstration of their dynamic stability on femtosecond scales, as well as the associated intense nanoscale electromagnetic fields, which are of particular interest to chiral, nonreciprocal light-mater interaction, are lacking. Here, we directly address these questions by reporting an analytical method for the generation of twisted skyrmion spin textures and their associated chiral electromagnetic fields at the core of plasmonic vortices, and their quantitative visualization through coherent nanofemto imaging by ITR-PEEM.[41,42] Our analytical model finds that the photonic spin-orbit interaction (SOI) within plasmonic vortices with quantized OAM of l=±1 molds the plasmonic SAM into a chiral skyrmion texture in the vacuum side, and a skyrmion counterpart of opposite topological charge in the metal side, whose cores host co-gyrating, anti-parallel in-plane E and B fields ($E{\cdot}B$ focus) that can drive magnetoelectric phenomena such as chiral axion electrodynamics.[43-45] Together, the

skyrmion pair forms a hedgehog spin texture within the primary vortex. The boundaries of the plasmonic spin skyrmion are defined by contours of linear polarization known as L-line singularities,[46,47] where atomically sharp superposition cat states of the plasmonic up- and down-spins are observed, which invite applications in quantum information processing at the atomic scale.[48,49] By recording the local field induced non-linear photoelectrons using ITR-PEEM with nanometer resolution and attosecond scanning accuracy,[42,50-52] we image the dynamical vectorial vortex fields, based on which we extract the plasmonic spin skyrmion textures,[53] skyrmion boundaries and topological charges, which are in quantitative agreement with our analytical model. The skyrmion topological character is also demonstrated to be stable longer than ~10 optical cycles, thus it can potentially function as information bits,[54-56] aid in Fourier optical processing,[57] transiently break the time reversal symmetry (TRS) to actuate coherent magnetoelectric devices,[44,58-61] and act as active nodes in quantum information storage and processing.[62]

II. Analytic Theory of Plasmonic SAM Skyrmions

A. Plasmonic vortices

SPPs are bound evanescent fields that propagate at metal/dielectric interfaces.[63] When circularly polarized light with helicity σ illuminates a sharp circular slit structure (see supplementary material Fig. S1), in an otherwise flat polycrystalline Ag film,[22] an SPP vortex with OAM of $l = \sigma$ is generated.[64] Equations (1a-c) describe the vectorial field components ($\boldsymbol{E}_z$, and $\boldsymbol{E}_{\parallel} = \boldsymbol{E}_r + \boldsymbol{E}_\theta$) of a plasmonic vortex carrying OAM of l that forms a phase singularity in E_z at the vortex core,[64-66] where r and θ represent the chosen cylindrical coordinates (see supplementary material):

$$E_z(r,\theta,0^+) = -E_0 \frac{2i^l \pi R k_{SPP}}{\omega_{SPP}\varepsilon_0\varepsilon_d} e^{ik_{SPP}R} e^{il\theta} J_l(k_{SPP}r) \quad (1a)$$

$$E_r(r,\theta,0^+) = E_0 \frac{i^l \pi \kappa}{\omega_{SPP}\varepsilon_0\varepsilon_d} e^{ik_{SPP}R} e^{il\theta} \left[2ir J_l(k_{SPP}r) - R\left(J_{l-1}(k_{SPP}r) - J_{l+1}(k_{SPP}r)\right)\right] (1b)$$

$$E_\theta(r,\theta,0^+) = -E_0 \frac{i^{l+1} \pi \kappa R}{\omega_{SPP}\varepsilon_0\varepsilon_d} e^{ik_{SPP}R} e^{il\theta} [J_{l-1}(k_{SPP}r) + J_{l+1}(k_{SPP}r)]. \quad (1c)$$

In eq.(1), 0^+ refers to the dielectric side, E_0 is the field amplitude which is normalized to 1 afterwards, ε_0 (ε_d) is the absolute (relative) bulk permittivity of the vacuum, $i = \sqrt{-1}$, ω_{SPP} is the SPP frequency, k_{SPP} and κ are the SPP wave vectors in-plane and normal to the interface, R is the radius of the coupling structure, and J_v is a Bessel function of order v that is defined by OAM of the orbiting E_z component, i.e., v=l (see supplementary material, and Fig. S1). Note that an imaginary part appears in eq. (1b), which accounts for the finite R, and causes the in-plane spin to twist, as will be shown later. In the following, we only consider the z=0^+ SPP field components at the interface, because they generate the 2PP signal that we image.

Pseudo color plots of the distribution of the field components from eqs. (1a-c) are shown in Figs. 1(a-c), for an l=-1 vortex with $R = 2\lambda_{SPP}$. The $|E_z|$ component has maximum at $r_1 \approx 0.29\lambda_{SPP} \approx 150$ nm for a plasmon wavelength λ_{SPP}=530 nm, to which we refer hereafter as the primary vortex ring [small dashed circle in Fig. 1(a)]. The superposed arrows in Fig. 1(a) indicate the in-plane Poynting vectors, corresponding to a counterclockwise (CCW) SPP propagation; the time evolution of the corresponding vortex field components are shown in Fig. S2. Moreover, while E_z vanishes at the vortex core where the phase is singular, a feature known as superoscillation,[67] the $|E_r|$ and $|E_\theta|$ have a strong focus, with $|E_r|$ passing through zero at r_1, and $|E_\theta|$ diminishing more slowly with r. The minimum of $|E_\theta|$ occurs at $r_2 \approx 0.61\lambda_{SPP}$.

A novel aspect of vortex fields that emerges from this analytical model, and which is likely to find important applications in magnetoelectric interactions and topology, is that vortex cores are the focus of $E \parallel B$ fields (Fig. S2). Although we do not experimentally image the plasmonic B field of the SPPs because of the lack of dipole interaction that can generate 2PP signal, their in-plane ($\boldsymbol{H}_\parallel = \boldsymbol{H}_r + \boldsymbol{H}_\theta$) components also form a focus at the vortex core, which resembles $\boldsymbol{E}_\parallel$, but have the *opposite* sign [SI eqs. (S4)]. Therefore, the surface parallel $\boldsymbol{E}_\parallel$ and $\boldsymbol{B}_\parallel = \mu\boldsymbol{H}_\parallel$ fields combine as a co-gyrating antiparallel pair in a tight focus at the vortex core. Like the photonic spin texture, the co-gyrating antiparallel relationship persists as long as the vortex is established. Due to the strong focusing of the in-plane fields, which drives the nonlinear photoemission, we expect vortex cores to be a focus of intense magnetoelectric coupling defined by the pseudoscalar $\boldsymbol{E}_\parallel \cdot \boldsymbol{B}_\parallel$ product. The calculated

distribution of $\boldsymbol{E}_{\parallel} \cdot \boldsymbol{B}_{\parallel}$ from the analytical model is shown in Fig. 1(d), where the anti-parallel $\boldsymbol{E}_{\parallel}$ and $\boldsymbol{B}_{\parallel}$ fields are focused on the $<\lambda_{SPP}/2$ length scale; the nanofemto distribution of the counterclockwise co-gyrating in-plane field vectors is shown in the SI movie 1. (Multimedia view) Note that the $\boldsymbol{E}_{\parallel}$ and $\boldsymbol{B}_{\parallel}$ fields become parallel and co-gyrate in a clockwise direction when the sign of vortex OAM is reversed.

The (anti)parallel context of the $\boldsymbol{E}_{\parallel}$ and $\boldsymbol{B}_{\parallel}$ fields at the vortex core is a consequence of focusing of circularly polarized light interacting by the circular coupling structure; it is thus a profoundly simple construct for interrogating magnetoelectric phenomena by ITR-PEEM and other near-field microscopic techniques. Moreover, such (anti)parallel E and B fields are a property of vortices composed of surface evanescent waves in general, where the associated transverse field forms a singularity at regions of the strong E∥B focus due to the cycloidal field polarization in the meridional plane. Therefore, such fields can also form in 2D semimetals/semiconductors where plasmon frequency is in the THz regime, or in 2D insulators in the form of phonon polaritons, etc.[20,68] Consequently, the E∥B focus can potentially drive magnetoelectric effect in a broad frequency regime, such as magnetoelectric coupling in metallic plasmonic nanoparticle dimers, where it drives coherently the light-nanostructure orientation-dependent magnetic and electric dipole chiral Raman spectra,[69] or excitation of magnetic moments parallel to the driving electric fields in bianisotropic metamaterials.[38,70-72] Finally, the strong E∥B may assist in the study of dynamical axion field θ through the topological magnetoelectric coupling $\theta \boldsymbol{E} \cdot \boldsymbol{B}$,[43,73-76] because it locally enhances the electromagnetic field strengths, breaks the TRS on subwavelength scale, and its frequency response can be tuned continuously to fall within the band gap of magnetically doped topological insulators.

B. Plasmonic SAM skyrmion

Having defined the vectorial SPP field vortex components in eqs. (1) and Fig. 1 for l=-1, we use them to calculate the associated SAM ($\boldsymbol{S}$) profile, defined as,[77,78]

$$\boldsymbol{S} \sim \frac{1}{4\omega} \mathrm{Im}[\varepsilon(\boldsymbol{E}^* \times \boldsymbol{E}) + \mu(\boldsymbol{H}^* \times \boldsymbol{H})] \quad (2)$$

where ω is frequency of the time-dependent electric $\boldsymbol{E}$ and magnetic $\boldsymbol{H}$ fields, and the asterisks indicate complex conjugation. According to the derived $\boldsymbol{E}$ and $\boldsymbol{H}$ field components (supplementary material), the vacuum SAM components for l=-1 are:

$$S_r(r,\theta,0^+) = \frac{8\pi^2 R^2 \kappa}{{\omega_{SPP}}^2 \varepsilon_0 \varepsilon_d} \frac{J_1^2(k_{SPP} r)}{r} \tag{3a}$$

$$S_\theta(r,\theta,0^+) = -\frac{8\pi^2 R r k_{SPP} \kappa}{{\omega_{SPP}}^2 \varepsilon_0 \varepsilon_d} J_1^2(k_{SPP} r) \tag{3b}$$

$$S_z(r,\theta,0^+) = 2\pi^2 R^2 \left(\frac{\kappa^2}{{\omega_{SPP}}^2 \varepsilon_0 \varepsilon_d} + \mu_0 \right) [J_0^2(k_{SPP} r) - J_2^2(k_{SPP} r)]. \tag{3c}$$

The S_z component is discontinuous, and on the metal side because (0^-) has an equivalent form, but the $\varepsilon_{\mathrm{d}} \to \varepsilon_{\mathrm{m}}$ (metallic permittivity) substitution below the plasma frequency, reverses its sign.

Based on eqs 3, we plot the normalized vacuum-side skyrmion SAM texture, $\boldsymbol{S_n} = \frac{\boldsymbol{S}}{|\boldsymbol{S}|}$ in Fig. 2(a). In this texture, vacuum SAM points up (+z) at the vortex core, aligning it with the SAM direction of the excitation light; moving away from the core, it continuously winds to the surface plane pointing away from the core at r_1, and finally down at its periphery at r_2,[79,80] as is illustrated in Fig. 2(b). At r_2, $S_{z,n}$, the z-component $\boldsymbol{S_n}$, has a π-phase reversal [Fig. 2(b) and Fig. 3(b)], such that the $S_{z,n}$ vectors on each side of r_2 are surface normal, but point in the opposite directions. We note, however, that the unnormalized spin, S_z, is continuous as it smoothly reverses direction upon crossing through zero at r_2.[7] The anti-parallel $S_{z,n}$ vectors across r_2 reflect the counterrotation of the in-plane fields that originate from the evanescent properties of SPPs. The superposition of the oppositely circulating in-plane fields at r_2 necessitates a transition through linear polarization, which is a chirality discontinuity catastrophe that occurs on the screening length scale where chiral interactions can achieve deep subwavelength contrast,[81-83] and the electron transport reciprocity is reversed.

The in-plane component of the normalized SAM, $\boldsymbol{S}_{\parallel,n} = \boldsymbol{S}_{r,n} + \boldsymbol{S}_{\theta,n}$ [arrows in Fig. 2(c)] has a phase that is spatially shifted from S_z by ~¼ λ_{SPP}. Consequently, its amplitude is zero at the vortex core and at r_2, but reaches maximum at r_1, as seen by the pseudoscalar plot of $|\boldsymbol{S}_{\parallel,\boldsymbol{n}}|$ in Fig. 2(c). Note that there is also a finite $\boldsymbol{S}_{\theta,n}$ proportional to R, which is evident as a twist of $\boldsymbol{S}_{\parallel,n}$ from the radial direction in Fig.

2(c). It appears because r is not negligible with respect to R in deriving the Bessel function orders. Therefore, the finite S_θ turns the SAM from a Néel- towards a twisted Bloch-type skyrmion texture when $r \sim R$.[80] The R-dependent SAM twist angle is quantified in supplementary material. Interestingly, plasmonic spin skyrmion textures possessing similar twisting characters have also been theoretically demonstrated to occur in chiral materials in between metallic films, but originating from a distinct mechanism.[84]

Similar to the interference of spin waves in magnetic skyrmion lattices, where a skyrmion unit is defined by a soliton solution of interfering waves with a defined wavelength,[85,86] we define a radius dependent skyrmion boundary based on the SPP interferences governed by the zeros of Bessel functions, and the Poincaré sphere of light polarization [Fig. 2(d)].[87,88] The first boundary is marked by the dashed circle of radius r_2 in Fig. 2(b,e). Such boundary is intrinsically associated with the second L-line polarization singularity fringe of the in-plane SPP fields. The L-line singularity[46] defines the interface where the $E_\parallel$ field is linearly polarized, and consequently, the out-of-plane SAM passes through $S_z = 0$. Mapping the SPP polarization onto a Poincaré polarization sphere, places the L-line at the equator, along which the linear $E_\parallel$ field polarization rotates by 2π [Fig. 2(d)]. From the Poincaré sphere perspective, the surface-normal positive and negative S_z components at the vortex core and at r_2, are the north and south poles, respectively, representing circular polarization, or C-point singularities;[46,47] the upper hemisphere bounded by the equator (r_1) encloses a half-skyrmion, or a meron [Fig. 2(d)].[22,23,89] Note that at L-lines, the out-of-plane SAM vanishes, while the in-plane SAM is maximum due to the momentum-SAM locking. We numerically compute the L-line and C-point distributions by calculating the ellipticity of the $E_\parallel$ fields, as shown in Fig. 2(e). The minimum ellipticity of 1 defines the C-point singularity at the vortex core [the center in Fig. 2(e)].[46,47] Away from the C-point, the SPP field becomes more elliptical, passing through linear at the first L-line singularity at r_1 [$S_z \to 0$ in Fig. 2(b)].

To evaluate the topological charge of the plasmonic SAM texture, we calculate the charge density, D, as defined by,[90]

$$D = \frac{1}{4\pi} \boldsymbol{S_n} \cdot \left(\frac{\partial \boldsymbol{S_n}}{\partial x} \times \frac{\partial \boldsymbol{S_n}}{\partial y} \right) \quad (4)$$

where the structure factor, $\boldsymbol{S_n}$, is the normalized SAM at each pixel in the Cartesian coordinates. The calculated areal distribution of D for the l=-1 vortex is shown in Fig. 2(f). Integration of *D* within the area defined by the second L-line [Fig. 2(e)] gives an integer topological charge of *N*=+1 for the l=-1 plasmonic vortex, confirming its skyrmion topological character.[24] For an l=+1 SPP vortex excited with right circularly polarized light, the topological charge is *N*=-1, due to the change in sign of the SAM pseudovectors.

The plasmonic skyrmion spin texture, defined here by the L-line and C-point analysis, establishes its homotopy to that of a twisted magnetic skyrmion,[46,47] and defines a precise method to locate both their dominant density (r_1) and boundary (r_2). Finally, because the plasmonic spin winding recurs along the radial direction as described by Bessel functions, the analysis of the topological texture based on eq. 4 can be extended outward from the vortex core.

C. Plasmonic SAM Hedgehog Texture

A notable aspect of plasmonic skyrmion SAM textures is that they form on both sides of the metal/vacuum interface, but with the opposite topological number according to the photonic spin topology across the interface described by a strong topological insulator $\mathbb{Z}_4$ index;[91-93] the interface-normal cross-section of the normalized SAM vectors $\boldsymbol{S_n}$ is shown in Fig. 3(a), and the vectorial spin components on vacuum and metal side of the interface are shown in Fig. 3(b) and (c), respectively. The $\boldsymbol{S_n}$ rotates by 2π with respect to the vortex core within r_1, because ε, and thus $S_z \sim \varepsilon(\boldsymbol{E}^* \times \boldsymbol{E})_z$, changes sign on an atomically sharp scale across the interface;[91] the in-plane SAM, which is locked to the CCW circulating k_{SPP}-vector, however, remains parallel across the interface. Within r_1, the combined spin texture of the two half-skyrmions form a hedgehog texture, which is homotopic to Berry curvature monopoles in topological materials,[74-76,94] magnetic monopole fields for electron vortex beam generation,[95,96] and spin monopoles in Bose-Einstein condensates[97] and photonic systems.[98] We note, however, the rate of spin texture winding is asymmetric across the interface, which is due to the joint electric and magnetic contributions to the total SAM (See supplementary material).

Unlike a macroscopic TRS breaking induced by a magnetic phase transition, for plasmonic vortices, the TRS is broken on λ_{SPP} length and the optical pulse time scales by a gyrating electron current that induces an inverse Faraday effect,[61] and the concomitant surface normal plasmonic SAM. Therefore, plasmonic spin hedgehog can potentially induce spin-Hall effect in transport of electrons on the ultrafast time scale.[99,100] Moreover, it may also act as sources of photoelectrons carrying OAM from the SPP field that is of interest for electron microscopy of magnetic materials.[96,101] We note that, compared to the in-plane skyrmion-anti-skyrmion pairs in magnetic materials,[102,103] the plasmonic skyrmion spin textures are more tightly confined at the quasi-2D metal/dielectric interfaces defined by the plasmon field decay.

III. Ultrafast Microscopy of Plasmonic Skyrmions

To validate the SAM skyrmion texture within an $|l|$=1 vortex core and its temporal structure, we record movies of the vectorial SPP vortex field dynamics by imaging the spatial distribution and temporal evolution of the 2PP signal by the ITR-PEEM method.[42,52] Figure 4(a) shows a schematic view of the ITR-PEEM experiment where two circularly polarized pulses of mutual delay τ illuminate a polycrystalline Ag film with a fabricated ring SPP coupling structure. The coupling structure causes the SPP field focusing with an orbital angular momentum defined both by the geometric charge of the coupling structure, and spin of the generating optical field. The as-recorded, one pulse, photoemission image obtained by left circularly polarized light excitation is shown in Fig. 4(b); the 2PP signal comes to an intense focus within a circular region of ~λ_{SPP} diameter centered on the vortex core. Excitation by light of the opposite handedness generates superficially the same 2PP distribution (See supplementary material). All SPP field components contribute to the total 2PP signal near the vortex core; this superposition of the in- and out-of-plane field-induced signals shrouds the SAM skyrmion, because one cannot immediately separate them.

The separate SPP field component-induced 2PP signals are obtained in an ITR-PEEM experiment by Fourier filtering (FT) the time-domain ITR-PEEM image sequence (See supplementary material).[25] This generates a phase dependent movie of the $|E_r|$ SPP field component oscillating at the laser driving frequency $1\omega_L$ (SI movie 2).

(Multimedia view) Figure 4(c) reports the Fourier filtered image of the $|E_r|$ component at τ~23.1 fs (τ =0 fs is defined by the pump-probe pulses' temporal overlap), where the image symmetrization and smoothing is applied as described in supplementary material. We further derive the $|E_z|$ and $|E_\theta|$ components from the E_r distribution,[53] by applying the Maxwell's equations and plot them in Fig. 4(d,e). The dashed circles in Fig. 4(c-e) mark the location of the vortex ring at $r_1 \approx 150$ nm, confirming agreement between the experiment and the analytical model [eqs. (2)]. Furthermore, from the experimental fields shown in Fig. 4(c-e), we construct the vectorial spin textures based on the corresponding Bessel function distributions. In Fig. 5(a), we show the derived distributions of $S_{z,n}$, and in Fig. 5(b) the magnitude and the directions of the normalized in-plane SAM components $S_{||,n}$ by a pseudo color map and arrows, respectively, which are in excellent agreement with the predicted distributions in Fig. 2(b,c). The observed continuous winding of $S_{z,n}$ from pointing up at the center to down at ~ r_2 , and in particular with the distinct twist of $S_{||,n}$ unambiguously confirm the generation of twisted skyrmion plasmonic spin texture at the l=-1 vortex. To avoid confusion, however, we do not directly image the SPP SAM, but our experiment enables to extract the vectorial fields, and based on the Maxwell's equations, to transform them into their consequent spin distributions.[25]

Moreover, the spin, and specifically, the inverse of the $|S_z|$, defines the in-plane SPP field ellipticity (L-line) distribution at the plasmonic vortex. Figure 5(c) shows the experimental ellipticity distribution of the l=-1 vortex, where distinct sharp contrast appears at both at r_1 and r_2, because the ellipticity becomes infinite and the SAM points in-plane. Such analysis locates the L-lines from the derived SAM textures. This L-line distribution agrees remarkably well with the calculated one in Fig. 2(e), to experimentally locate the stable skyrmion texture that is bounded by the 2nd L-line from the vortex core. Conclusive experimental evidence of the topological texture assignment is shown in Fig. 5(d), where the L-line distribution (blue) is plotted, along with the integrated topological charge density (red) as a function the integration radius. Horizontal black dashed lines indicating the location of integer topological charges are also shown intersecting with the even-numbered L-lines, in agreement with the numerical calculations shown by corresponding dashed curves in Fig. 5(d).

Therefore, the even-numbered L-lines naturally define boundaries separating quantized integer increments in the topological charge that confirm the homotopy of the SAM skyrmion textures. The odd L-lines, however, mark the half-skyrmion, or meron textures, where the quasiparticle density [Fig. 2(f)], and thus the topological charge varies the most rapidly.

Finally, with the capability of resolving SPP vortex field dynamics supporting the spin skyrmion quasiparticle with nanofemto precision, we demonstrate that such quasiparticle is stable over the SPP pulse duration. Figure 5(e) plots the spin skyrmion topological charge as a function of inter-pulse delay τ in unit of optical cycles; the integer topological charge is observed to stabilize after ~20 fs when the SPP vortex is fully established, and then remains constant for over ~10 optical cycles (~18 fs) before it dissolves. Therefore, such dynamic spin quasiparticle, which break the TRS on deep subwavelength scale, can serve pulses of transient magnetization at THz frequencies, that can actuate the inverse Faraday effect or ultrafast spin-dependent electron transport switching. The temporal stability of topological charge is defined by the generation pulse width, and thus can be set by illumination with circularly polarized fields of any duration. To exist in absence of the generating electromagnetic field, as does the magnetic skyrmion, would require the magnetic monopole spin texture to be prepared by other means.

IV. Conclusions

Our study unambiguously demonstrates, with nanofemto resolution, an ultrafast twisted plasmonic SAM skyrmion texture, its sub-diffraction limited polarization L-line singularity boundaries, and integer topological character, which are dynamically stable on ~20 fs time scale of the generation pulse duration. In addition, our model also finds that, 1) there exists an intense focus of the $E_{||} \cdot B_{||}$ term that is of potential interest for nonlinear magnetoelectric couplings and axion field dynamics in quantum materials,[43,73,104] and 2) a pair of skyrmions of opposite charge are generated across the SPP supporting interface, where within the primary vortex ring the plasmonic spin can be considered as a monopole-like hedgehog texture, and can induce a transient spin-Hall effect.[99,100] The topological spin textures generated by the interaction of

optical fields with OAM structures that induce polaritonic spin-orbit interaction is a general phenomenology of focusing of polaritonic fields that carry OAM.[20] Finally, because the reported plasmonic skyrmion is delivered by intense plasmonic fields concentrated on the λ_{SPP} scale, it is expected to imprint its topological spin texture and OAM on topologically trivial or nontrivial materials[105,106] on femtosecond time scale. Thus, the SAM skyrmions are ideal for provoking topological quasi-energy states by Floquet engineering, and texturing of spins by Poincaré engineering to achieve TRS breaking, and nonreciprocal physics in the condensed quantum matter.[38,39,43,107,108]

Supplementary Materials

See supplementary materials for detailed derivations of the twisted plasmonic skyrmion textures, as well as the processing and analysis of the ITR-PEEM data. Figures S1-S6, Movies S1 and S2. (Multimedia view)

Acknowledgements

This research was supported by the NSF Center for Chemical Innovation on Chemistry at the Space-Time Limit grant CHE-1414466 and ONR MURI Grant No. N00014-20-S-F00. YD thanks R. Mong for consultation on the analytical theory; HP thanks V. Liu and V. A. Apkarian for discussion of magnetoelectric effects and axion physics.

Author Declarations

Conflict of Interest

The authors have no competing interests.

Author Contributions

Author contributions: YD performed the analytical modeling and experiments; ZZ, AG, and KK contributed to the nanofabrication, electromagnetic simulation, and laser operation; MD supervised the establishment of the ITR-PEEM experiment; AK advised on the ITR-PEEM measurements and data analysis; CBH introduced and guided the research on topological plasmonics; HP supervised the research; YD and HP wrote the manuscript.

Data availability

The theoretical simulations results and experimental ITR-PEEM data are available from the authors upon request. The analytical model of topological skyrmion field textures is presented in the paper, and the supplementary material.

References:

[1] T. W. B. Kibble, Phys. Rep. **67**, 183 (1980).
[2] W. H. Zurek, Phys. Rep. **276**, 177 (1996).
[3] F. Duncan and M. Haldane, Rev. Mod. Phys. **89**, 040502 (2017).
[4] L. Dominici, G. Dagvadorj, J. M. Fellows, D. Ballarini, M. De Giorgi, F. M. Marchetti, B. Piccirillo, L. Marrucci, A. Bramati, G. Gigli, M. H. Szymanska and D. Sanvitto, Sci. Adv. **1**, e1500807 (2015).
[5] A. Duzgun, J. V. Selinger and A. Saxena, Phys. Rev. B **97**, 062706 (2018).
[6] Y. Shen, X. Wang, Z. Xie, C. Min, X. Fu, Q. Liu, M. Gong and X. Yuan, Light Sci. Appl. **8**, 1 (2019).
[7] L. P. Du, A. P. Yang, A. V. Zayats and X. C. Yuan, Nat. Phys. **15**, 650 (2019).
[8] T. H. R. Skyrme, Nucl. Phys. **31**, 556 (1962).
[9] S. Muhlbauer, B. Binz, F. Jonietz, C. Pfleiderer, A. Rosch, A. Neubauer, R. Georgii and P. Boni, Science **323**, 915 (2009).
[10] Y. Fujishiro, N. Kanazawa, T. Nakajima, X. Z. Yu, K. Ohishi, Y. Kawamura, K. Kakurai, T. Arima, H. Mitamura, A. Miyake, K. Akiba, M. Tokunaga, A. Matsuo, K. Kindo, T. Koretsune, R. Arita and Y. Tokura, Nat. Commun. **10**, 1059 (2019).
[11] U. Al Khawaja and H. Stoof, Nature **411**, 918 (2001).
[12] S. Donati, L. Dominici, G. Dagvadorj, D. Ballarini, M. De Giorgi, A. Bramati, G. Gigli, Y. G. Rubo, M. H. Szymanska and D. Sanvitto, Proc. Natl. Acad. Sci. U.S.A. **113**, 14926 (2016).
[13] D. C. Wright and N. D. Mermin, Rev. Mod. Phys. **61**, 385 (1989).
[14] Y. Shen, Y. Hou, N. Papasimakis and N. I. Zheludev, Nat. Commun. **12**, 5891 (2021).
[15] S. J. Gao, F. C. Speirits, F. Castellucci, S. Franke-Arnold, S. M. Barnett and J. B. Gotte, Phys. Rev. A **102**, 053513 (2020).
[16] R. Gutierrez-Cuevas and E. Pisanty, J. Opt. **23**, 024004 (2021).
[17] J. Zhu, S. Liu and Y.-S. Zhang, arXiv preprint arXiv:2103.11293(2021).
[18] S. Tsesses, E. Ostrovsky, K. Cohen, B. Gjonaj, N. H. Lindner and G. Bartal, Science **361**, 993 (2018).
[19] T. J. Davis, D. Janoschka, P. Dreher, B. Frank, F. J. Meyer Zu Heringdorf and H. Giessen, Science **368**, eaba6415 (2020).
[20] L. Xiong, Y. Li, D. Halbertal, M. Sammon, Z. Sun, S. Liu, J. H. Edgar, T. Low, M. M. Fogler, C. R. Dean, A. J. Millis and D. N. Basov, Nano Lett. **21**, 9256 (2021).
[21] P. Shi, L. P. Du and X. C. Yuan, Nanophotonics **10**, 3927 (2021).
[22] Y. Dai, Z. Zhou, A. Ghosh, R. S. K. Mong, A. Kubo, C. B. Huang and H. Petek, Nature

588, 616 (2020).
[23] A. Ghosh, S. N. Yang, Y. A. Dai, Z. K. Zhou, T. Y. Wang, C. B. Huang and H. Petek, Appl. Phys. Rev. **8**, 041413 (2021).
[24] N. Nagaosa and Y. Tokura, Nat. Nanotechnol. **8**, 899 (2013).
[25] Y. Dai, Z. Zhou, A. Ghosh, S. Yang, C. B. Huang and H. Petek, MRS Bulletin **46**, 1 (2021).
[26] J. Watzel and J. Berakdar, Phys. Rev. A **102**, 063105 (2020).
[27] C. Caloz, A. Alu, S. Tretyakov, D. Sounas, K. Achouri and Z. L. Deck-Leger, Phys. Rev. App. **10**, 047001 (2018).
[28] Y. Tokura and N. Nagaosa, Nat. Commun. **9**, 3740 (2018).
[29] S. H. Gong, F. Alpeggiani, B. Sciacca, E. C. Garnett and L. Kuipers, Science **359**, 443 (2018).
[30] S. A. Vitale, D. Nezich, J. O. Varghese, P. Kim, N. Gedik, P. Jarillo-Herrero, D. Xiao and M. Rothschild, Small **14**, e1801483 (2018).
[31] T. Chervy, S. Azzini, E. Lorchat, S. J. Wang, Y. Gorodetski, J. A. Hutchison, S. Berciaud, T. W. Ebbesen and C. Genet, ACS Photonics **5**, 1281 (2018).
[32] G. Hu, X. Hong, K. Wang, J. Wu, H.-X. Xu, W. Zhao, W. Liu, S. Zhang, F. Garcia-Vidal and B. Wang, Nat. Photonics **13**, 467 (2019).
[33] N. H. Lindner, G. Refael and V. Galitski, Nat. Phys. **7**, 490 (2011).
[34] M. A. Sentef, M. Claassen, A. F. Kemper, B. Moritz, T. Oka, J. K. Freericks and T. P. Devereaux, Nat. Commun. **6**, 7047 (2015).
[35] R. Zhang, Y. Zhang, Z. C. Dong, S. Jiang, C. Zhang, L. G. Chen, L. Zhang, Y. Liao, J. Aizpurua, Y. Luo, J. L. Yang and J. G. Hou, Nature **498**, 82 (2013).
[36] A. Pham, A. Zhao, C. Genet and A. Drezet, Phys. Rev. A **98**, 013837 (2018).
[37] J. Lee, K. T. Crampton, N. Tallarida and V. A. Apkarian, Nature **568**, 78 (2019).
[38] T. Ozawa, H. M. Price, A. Amo, N. Goldman, M. Hafezi, L. Lu, M. C. Rechtsman, D. Schuster, J. Simon, O. Zilberberg and I. Carusotto, Rev. Mod. Phys. **91**, 015006 (2019).
[39] D. Smirnova, D. Leykam, Y. D. Chong and Y. Kivshar, Appl. Phys. Rev. **7**, 021306 (2020).
[40] T. Van Mechelen and Z. Jacob, Phys. Rev. B **99**, 205146 (2019).
[41] A. Kubo, N. Pontius and H. Petek, Nano Lett. **7**, 470 (2007).
[42] M. Dąbrowski, Y. Dai and H. Petek, Chem. Rev. **120**, 6247 (2020).
[43] D. M. Nenno, C. A. C. Garcia, J. Gooth, C. Felser and P. Narang, Nat. Rev. Phys. **2**, 682 (2020).
[44] S. Zhong, J. Orenstein and J. E. Moore, Phys. Rev. Lett. **115**, 117403 (2015).
[45] A. M. Essin, J. E. Moore and D. Vanderbilt, Phys. Rev. Lett. **102**, 146805 (2009).
[46] T. Fosel, V. Peano and F. Marquardt, New. J. Phys. **19**, 115013 (2017).
[47] M. V. Berry and M. R. Dennis, Proc. Roy. Soc. a-Math. Phys. **457**, 141 (2001).
[48] S. Mukamel, M. Freyberger, W. Schleich, M. Bellini, A. Zavatta, G. Leuchs, C. Silberhorn, R. W. Boyd, L. L. Sanchez-Soto, A. Stefanov, M. Barbieri, A. Paterova, L. Krivitsky, S. Shwartz, K. Tamasaku, K. Dorfman, F. Schlawin, V. Sandoghdar, M. Raymer, A. Marcus, O. Varnavski, T. Goodson, Z. Y. Zhou, B. S. Shi, S. Asban, M. Scully, G. Agarwal, T. Peng, A. V. Sokolov, Z. D. Zhang, M. S. Zubairy, I. A. Vartanyants, E. del Valle and F. Laussy, J. Phys. B **53**, 072002 (2020).
[49] D. Peller, C. Roelcke, L. Z. Kastner, T. Buchner, A. Neef, J. Hayes, F. Bonafé, D.

Sidler, M. Ruggenthaler and A. Rubio, Nat. Photonics **15**, 143 (2021).
[50] D. Podbiel, P. Kahl, A. Makris, B. Frank, S. Sindermann, T. J. Davis, H. Giessen, M. H. Hoegen and F. J. Meyer Zu Heringdorf, Nano Lett. **17**, 6569 (2017).
[51] G. Spektor, D. Kilbane, A. K. Mahro, M. Hartelt, E. Prinz, M. Aeschlimann and M. Orenstein, Phys. Rev. X **9**, 021031 (2019).
[52] M. Dąbrowski, Y. Dai and H. Petek, J. Phys. Chem. Lett. **8**, 4446 (2017).
[53] E. Ostrovsky, K. Cohen, S. Tsesses, B. Gjonaj and G. Bartal, Optica **5**, 283 (2018).
[54] H. Rubinsztein-Dunlop, A. Forbes, M. V. Berry, M. R. Dennis, D. L. Andrews, M. Mansuripur, C. Denz, C. Alpmann, P. Banzer and T. Bauer, J. Opt. **19**, 013001 (2016).
[55] C. Monroe, Nature **416**, 238 (2002).
[56] M. S. Tame, K. R. McEnery, S. K. Ozdemir, J. Lee, S. A. Maier and M. S. Kim, Nat. Phys. **9**, 329 (2013).
[57] B. Muminov and L. T. Vuong, Optica **7**, 1079 (2020).
[58] A. V. Kimel, A. Kirilyuk, P. A. Usachev, R. V. Pisarev, A. M. Balbashov and T. Rasing, Nature **435**, 655 (2005).
[59] A. Dutta, A. V. Kildishev, V. M. Shalaev, A. Boltasseva and E. E. Marinero, Opt. Mater. Express **7**, 4316 (2017).
[60] J. Hurst, P. M. Oppeneer, G. Manfredi and P.-A. Hervieux, Phys. Rev. B **98**, 134439 (2018).
[61] O. H. C. Cheng, D. H. Son and M. Sheldon, Nat. Photonics **14**, 365 (2020).
[62] H. Wei, Z. Wang, X. Tian, M. Kall and H. Xu, Nat. Commun. **2**, 387 (2011).
[63] J. Pitarke, V. Silkin, E. Chulkov and P. Echenique, Rep. Prog. Phys. **70**, 1 (2006).
[64] S. Yang, W. Chen, R. L. Nelson and Q. Zhan, Opt. Lett. **34**, 3047 (2009).
[65] H. Kim, J. Park, S.-W. Cho, S.-Y. Lee, M. Kang and B. Lee, Nano Lett. **10**, 529 (2010).
[66] Y. Gorodetski, A. Niv, V. Kleiner and E. Hasman, Phys. Rev. Lett. **101**, 043903 (2008).
[67] M. Berry, N. Zheludev, Y. Aharonov, F. Colombo, I. Sabadini, D. C. Struppa, J. Tollaksen, E. T. Rogers, F. Qin and M. Hong, J. Opt. **21**, 053002 (2019).
[68] D. N. Basov, M. M. Fogler and F. J. García de Abajo, Science **354**, aag1992 (2016).
[69] M. Banik, K. Rodriguez, E. Hulkko and V. A. Apkarian, ACS Photonics **3**, 2482 (2016).
[70] T. G. Mackay and A. Lakhtakia. *Electromagnetic anisotropy and bianisotropy: a field guide*. World Scientific. 1-31 (2019).
[71] V. S. Asadchy, A. Diaz-Rubio and S. A. Tretyakov, Nanophotonics **7**, 1069 (2018).
[72] S. A. H. Gangaraj, M. G. Silveirinha and G. W. Hanson, IEEE J. Multiscale Multiphys. Comput. Tech. **2**, 3 (2017).
[73] J. Gooth, B. Bradlyn, S. Honnali, C. Schindler, N. Kumar, J. Noky, Y. Qi, C. Shekhar, Y. Sun and Z. Wang, Nature **575**, 315 (2019).
[74] X.-L. Qi, R. Li, J. Zang and S.-C. Zhang, Science **323**, 1184 (2009).
[75] X.-L. Qi and S.-C. Zhang, Rev. Mod. Phys. **83**, 1057 (2011).
[76] M. Z. Hasan and C. L. Kane, Rev. Mod. Phys. **82**, 3045 (2010).
[77] K. Y. Bliokh, A. Y. Bekshaev and F. Nori, Nat. Commun. **5**, 3300 (2014).
[78] T. Van Mechelen and Z. Jacob, Optica **3**, 118 (2016).
[79] S. Zhang, G. van der Laan, J. Muller, L. Heinen, M. Garst, A. Bauer, H. Berger, C. Pfleiderer and T. Hesjedal, Proc. Natl. Acad. Sci. U.S.A. **115**, 6386 (2018).

[80] S. L. Zhang, G. van der Laan, W. W. Wang, A. A. Haghighirad and T. Hesjedal, Phys. Rev. Lett. **120**, 227202 (2018).
[81] M. V. Berry and M. R. Dennis, Proc. Roy. Soc. a-Math. Phys. **459**, 1261 (2003).
[82] L. Wei, A. V. Zayats and F. J. Rodriguez-Fortuno, Phys. Rev. Lett. **121**, 193901 (2018).
[83] J. Pollard, G. Posnjak, S. Čopar, I. Muševič and G. P. Alexander, Phys. Rev. X **9**, 021004 (2019).
[84] Q. Zhang, Z. Xie, L. Du, P. Shi and X. Yuan, Phys. Rev. Res. **3**, 023109 (2021).
[85] A. N. Bogdanov and C. Panagopoulos, Phys. Today **73**, 44 (2020).
[86] A. Rosch, Nat. Mater. **15**, 1231 (2016).
[87] Y. Shen, Opt. Lett. **46**, 3737 (2021).
[88] Y. Shen, E. C. Martínez and C. Rosales-Guzmán, ACS Photonics **9**, 296 (2022).
[89] X. Z. Yu, W. Koshibae, Y. Tokunaga, K. Shibata, Y. Taguchi, N. Nagaosa and Y. Tokura, Nature **564**, 95 (2018).
[90] S. Heinze, K. von Bergmann, M. Menzel, J. Brede, A. Kubetzka, R. Wiesendanger, G. Bihlmayer and S. Blugel, Nat. Phys. **7**, 713 (2011).
[91] K. Y. Bliokh, D. Leykam, M. Lein and F. Nori, Nat. Commun. **10**, 580 (2019).
[92] P. Shi, L. Du, C. Li, A. V. Zayats and X. Yuan, Proc. Natl. Acad. Sci. U.S.A. **118**, e2018816118 (2021).
[93] E. Khalaf, H. C. Po, A. Vishwanath and H. Watanabe, Phys. Rev. X **8**, 031070 (2018).
[94] S.-Y. Xu, M. Neupane, C. Liu, D. Zhang, A. Richardella, L. Andrew Wray, N. Alidoust, M. Leandersson, T. Balasubramanian, J. Sánchez-Barriga, O. Rader, G. Landolt, B. Slomski, J. Hugo Dil, J. Osterwalder, T.-R. Chang, H.-T. Jeng, H. Lin, A. Bansil, N. Samarth and M. Zahid Hasan, Nat. Phys. **8**, 616 (2012).
[95] A. Beche, R. Van Boxem, G. Van Tendeloo and J. Verbeeck, Nat. Phys. **10**, 26 (2014).
[96] S. M. Lloyd, M. Babiker, G. Thirunavukkarasu and J. Yuan, Rev. Mod. Phys. **89**, 035004 (2017).
[97] M. W. Ray, E. Ruokokoski, S. Kandel, M. Mottonen and D. S. Hall, Nature **505**, 657 (2014).
[98] T. Van Mechelen and Z. Jacob, Opt. Mater. Express **9**, 95 (2019).
[99] Y. Tokura, M. Kawasaki and N. Nagaosa, Nat. Phys. **13**, 1056 (2017).
[100] K. Y. Bliokh, I. P. Ivanov, G. Guzzinati, L. Clark, R. Van Boxem, A. Beche, R. Juchtmans, M. A. Alonso, P. Schattschneider, F. Nori and J. Verbeeck, Phys. Rep. **690**, 1 (2017).
[101] C. L. Jia, D. C. Ma, A. F. Schaffer and J. Berakdar, J. Opt. **21**, 124001 (2019).
[102] U. Ritzmann, S. von Malottki, J.-V. Kim, S. Heinze, J. Sinova and B. Dupé, Nat. Electron. **1**, 451 (2018).
[103] M. Stier, W. Häusler, T. Posske, G. Gurski and M. Thorwart, Phys. Rev. Lett. **118**, 267203 (2017).
[104] L. Wu, M. Salehi, N. Koirala, J. Moon, S. Oh and N. P. Armitage, Science **354**, 1124 (2016).
[105] T. Eggebrecht, M. Moller, J. G. Gatzmann, N. Rubiano da Silva, A. Feist, U. Martens, H. Ulrichs, M. Munzenberg, C. Ropers and S. Schafer, Phys. Rev. Lett. **118**, 097203 (2017).
[106] G. Berruto, I. Madan, Y. Murooka, G. M. Vanacore, E. Pomarico, J. Rajeswari, R.

Lamb, P. Huang, A. J. Kruchkov, Y. Togawa, T. LaGrange, D. McGrouther, H. M. Ronnow and F. Carbone, Phys. Rev. Lett. **120**, 117201 (2018).

[107] M. Claassen, D. M. Kennes, M. Zingl, M. A. Sentef and A. Rubio, Nat. Phys. **15**, 766 (2019).

[108] H. Liu, J. T. Sun, C. C. Song, H. Q. Huang, F. Liu and S. Meng, Chin. Phys. Lett. **37**, 067101 (2020).

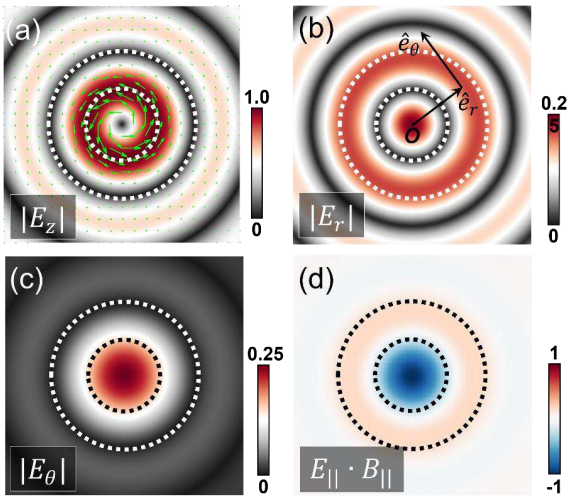

Figure 1. Vectorial plasmonic vortex fields. a) The calculated $|E_z|$ normalized component (color scale) of the SPP field generated by illumination of the coupling structure with counterclockwise (left) circularly polarized σ=-1 light; the small dashed circle (also, in Fig. 2 and Fig. 4) marks the first maximum of $|E_z|$ at $r_1 \approx$150 nm (the primary vortex ring). The field forms a vortex with a phase singularity at its core, where destructive interference sets $|E_z| = 0$. The green arrows indicate the in-plane Poynting vectors near r_1 for l=-1. b) The contributions to the $|E_r|$ field, being spatially shifted by ¼ of the Bessel function modulation from E_z, interfere constructively at the vortex core, and destructively at r_1. The unit vectors, $\hat{e}_r$ and $\hat{e}_\theta$, indicate the polar coordinates of the in-plane fields with origin at the vortex core. c) The $|E_\theta|$ field is less tightly focused at the core than $|E_r|$, and decays in outward direction more slowly. The color scales showing the normalized field amplitudes of

b) and c) are amplified 4x with respect to a). d) The distribution of magnetoelectric coupling pseudoscalar $\boldsymbol{E}_{\parallel} \cdot \boldsymbol{B}_{\parallel}$ normalized by the ($|\boldsymbol{E}_{\parallel}||\boldsymbol{B}_{\parallel}|$) field amplitudes at the vortex core.

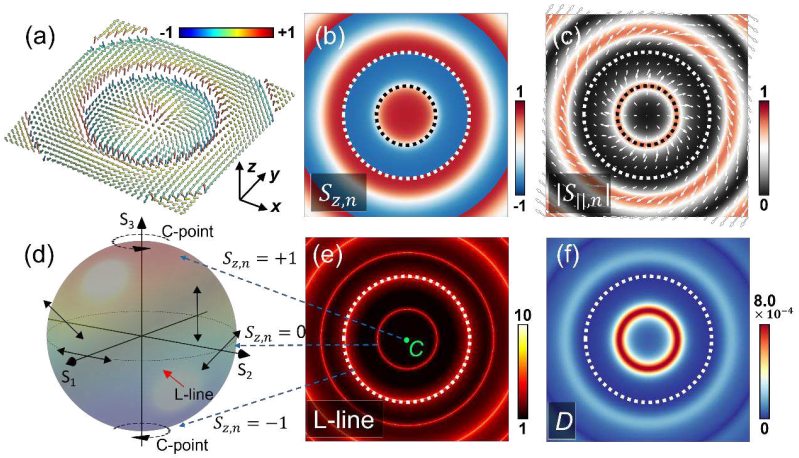

Figure 2. Plasmonic spin skyrmion texture and its polarization singularity boundary. a) A 3D representation of SAM at the vortex of an l=-1 plasmonic skyrmion. The color scale indicates the amplitude of $S_{z,n}$. b) and c) 2D representations, where the color scales indicate the amplitude of $S_{z,n}$ and $S_{\parallel,n}$, which are maximized at the vortex core and edge, and vortex ring at r_1, respectively. The arrows in c) indicate the $S_{\parallel,n}$ directions. d) Poincaré sphere of the SPP field polarization, where $S_{1\text{-}3}$ axes are the polarization Stokes parameters. The red arrow indicates the equator, which defines the SPP field polarizations at the L-line singularity, along which the linear polarization rotates by 2π. The north and south poles correspond to the C-point singularities that define the core and boundary of the plasmonic SAM skyrmion. e) A map of the L-line singularities, where the bright contrast rings, centered on the C-point singularity (marked by C) at the vortex core, identify interfaces where the in-plane plasmonic fields are linearly polarized corresponding to equators of the Poincaré sphere. The inner L-line ring occurs at r_1, where the skyrmion density is also maximum, while the second one forms the skyrmion boundary at r_2. The L-line

singularities that repeat beyond r_2, alternate between defining the skyrmion density maxima, and boundaries. Blue dashed arrows indicate the correspondence of the L-line and C-point features with the Poincaré sphere. f) The calculated plasmonic skyrmion density *D* distribution, which peaks at r_1 where $S_z = 0$. The black dashed circles in b), c), and the white dashed circles in b), c), e), f) indicate the primary vortex ring at r_1 and skyrmion boundary at r_2, respectively.

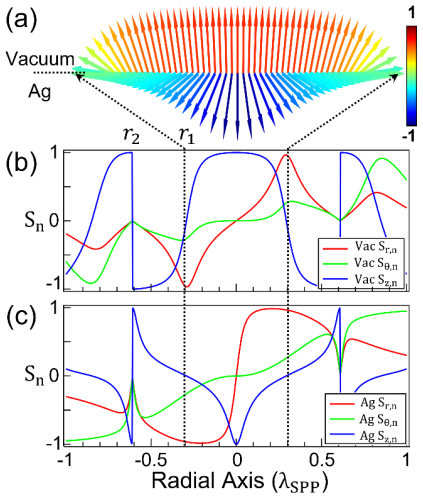

Figure 3. Plasmonic spin hedgehog texture. a) SAM hedgehog profile across the dielectric/metal interface. The color scale indicates the $S_{z,n}$ magnitude. b) The vacuum (Vac), and c) metal (Ag) radial variation of the normalized SAM components in the cylindrical coordinates.

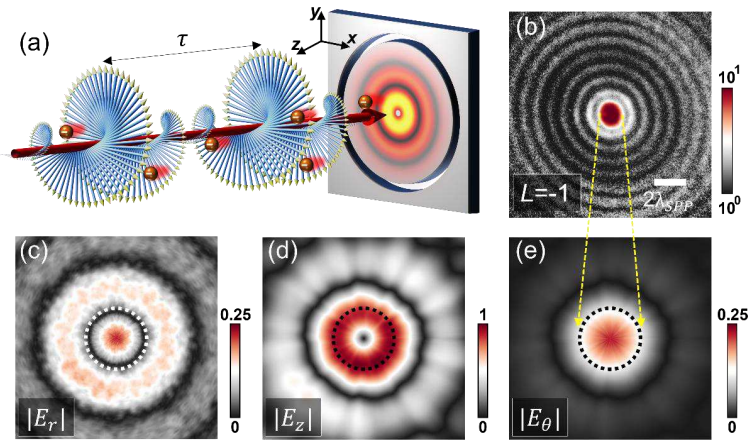

Figure 4. Ultrafast vectorial imaging of the plasmonic vortex fields. a) Schematic of the ITR-PEEM experiment.[42] Circularly polarized pump-probe pulse pairs focused through the PEEM electron objective lens onto the sample (right square), launch SPP waves depicted as concentric red contrast. The intensified SPP field at the coupling structure center excites 2PP of electrons (red spheres) that are collected and imaged by the PEEM electron optics. Only single circular coupling structure is shown. b) One pulse as-recorded PEEM image showing static distributions of the 2PP signal from l=-1 plasmonic vortices with R=5λ_{SPP}, in a logarithmic color scale to show the 2PP signal from the vortex beyond its core. The logarithmic 2PP intensities are normalized to 1. c) $|E_r|$ component of the SPP vortex at τ~23.1 fs extracted by IFT of the $1\omega_L$ component of the ITR-PEEM movie taken with two pulses. d), e) The derived $|E_z|$ and $|E_\theta|$ components from c). The color scales report the normalized field strengths; the dashed circles in (c-e) indicate the vortex ring at r_1, representing a zoomed in region from b) as indicated by the yellow arrows. The field amplitudes in (c-e) are normalized to the maximum of the $|E_z|$ field along the primary vortex ring. The lateral dimensions of experimental images in (c-e) are $2\lambda_{SPP}$.

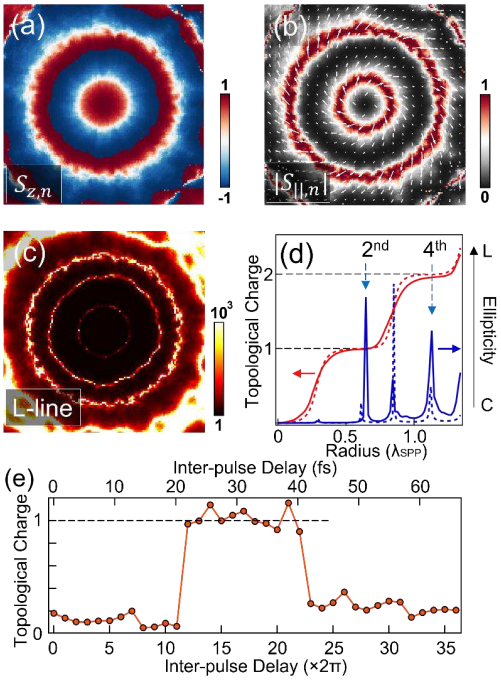

Figure 5. Experimental reconstruction of plasmonic spin skyrmion texture and its topological, and temporal properties. a), b) Normalized $S_{z,n}$ and $|S_{||,n}|$ spin components derived from the experimentally observed vectorial fields, corresponding to those from the analytical model in Fig. 2b,c. The arrows in b) represent the directions of the normalized in-plane SAM vectors. c) Experimental ellipticity (L-line) distribution obtained from $1/|S_z|$, indicating the characteristic domains within which the topological charge increases by half-integer quanta traversing each L-line. The lateral dimensions of (a-c) are $2\lambda_{SPP}$. d) Experimentally (solid) and numerically (dashed) integrated topological charge density (red) as a function of the radius of the circular integration domain, calculated by the integration of topological charge density *D* (normalized by 4π) within the corresponding radius, along with the calculated radius dependent ellipticity (blue) representing polarization states from circular (C; minimum) to linear (L; maximum). The topological charge increases by integer |1| quanta, as marked by the horizontal dashed lines, when the radius approaches to a skyrmion boundary. The spatial

PLEASE CITE THIS ARTICLE AS DOI: 10.1063/5.0084482

coordinates of the even-number L-lines are determined by zeros of eq. 3c. e) the experimentally derived topological charge of the plasmonic spin skyrmion quasiparticle as a function of inter-pulse delay in unit of fs and optical cycles. Integer character becomes stabilized at around ~10 optical cycles, when the SPP vortex is fully established, and remains constant for another ~10 optical cycles before the vortex dissolves.

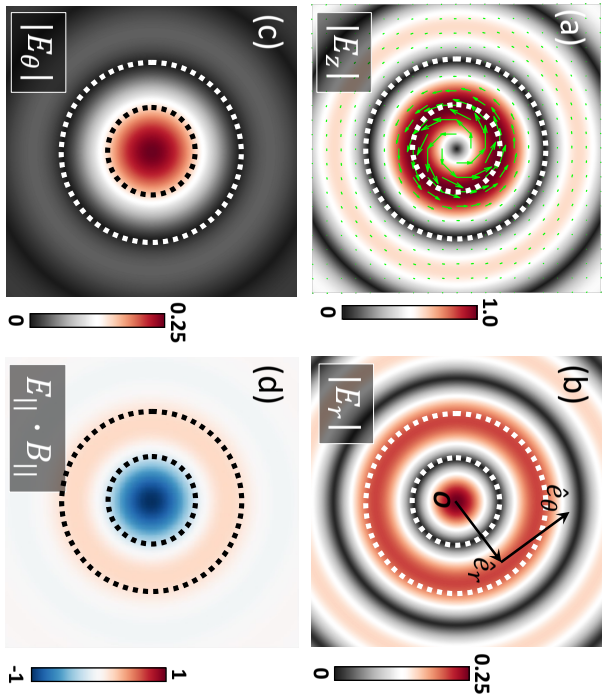

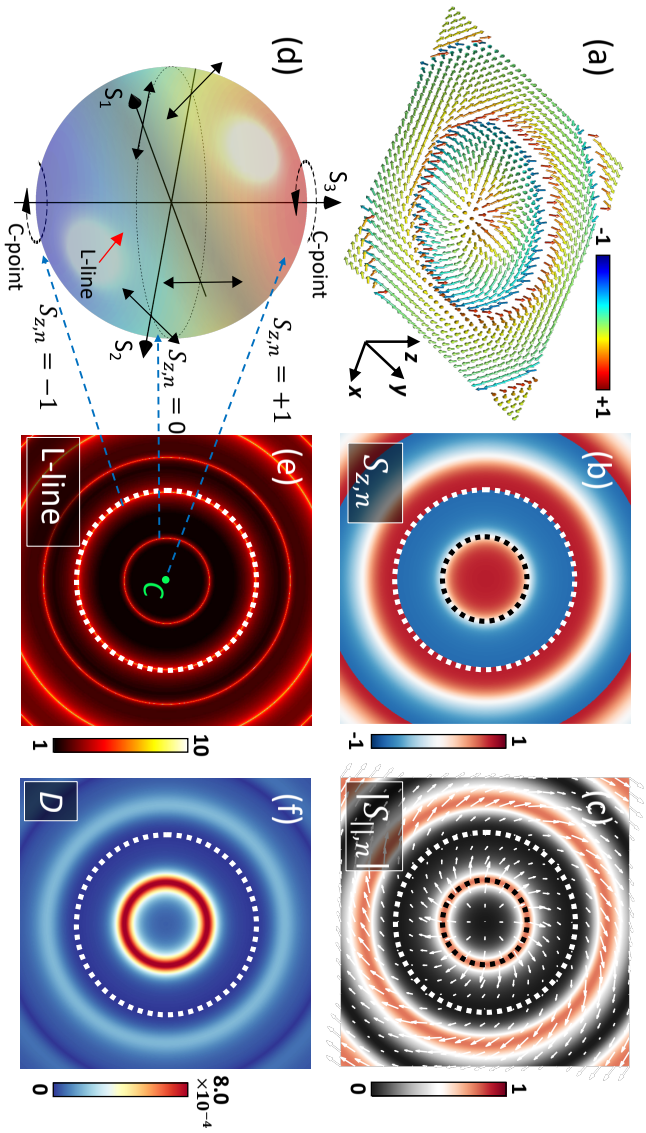

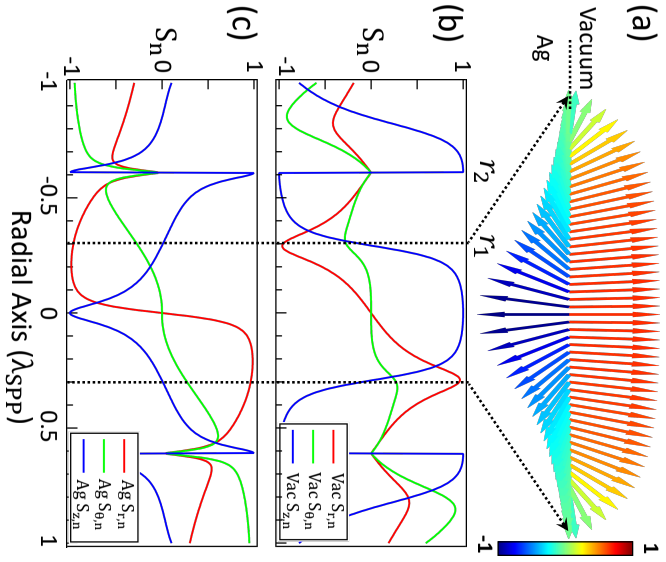

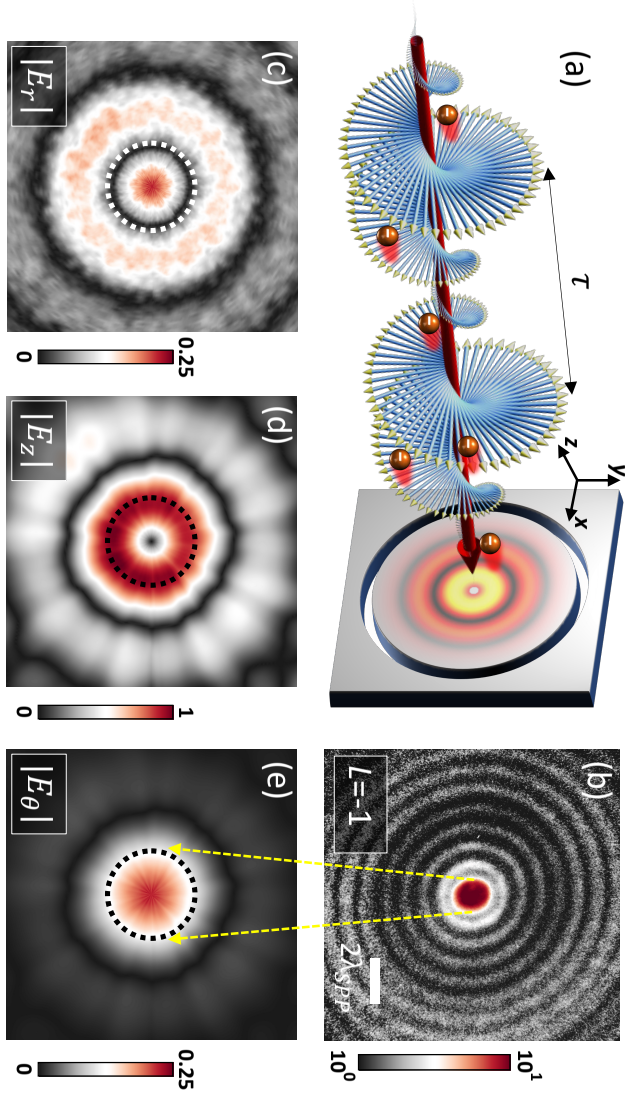

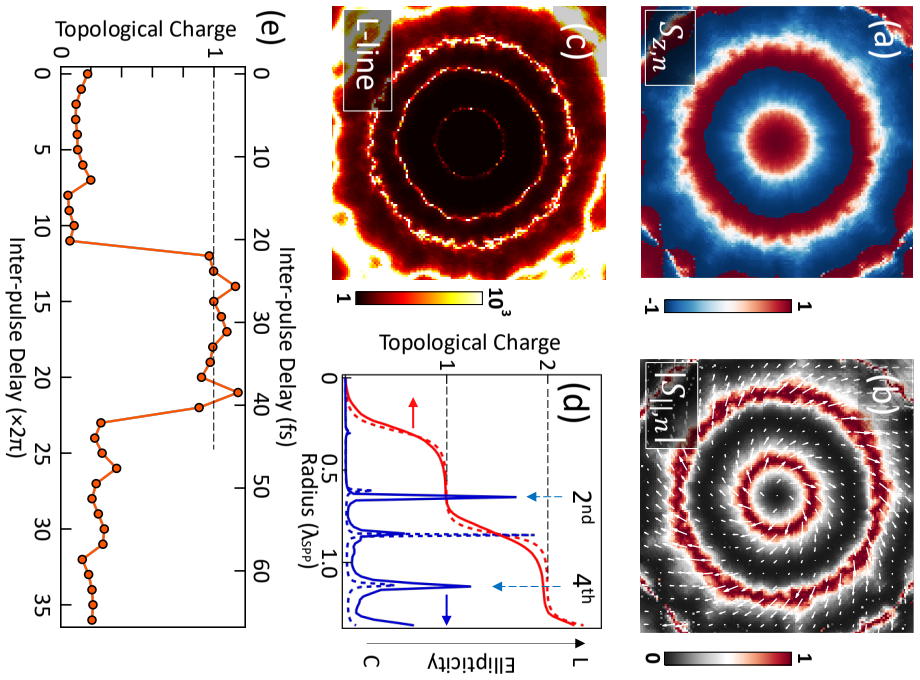

PLEASE CITE THIS ARTICLE AS DOI: 10.1063/5.0084482

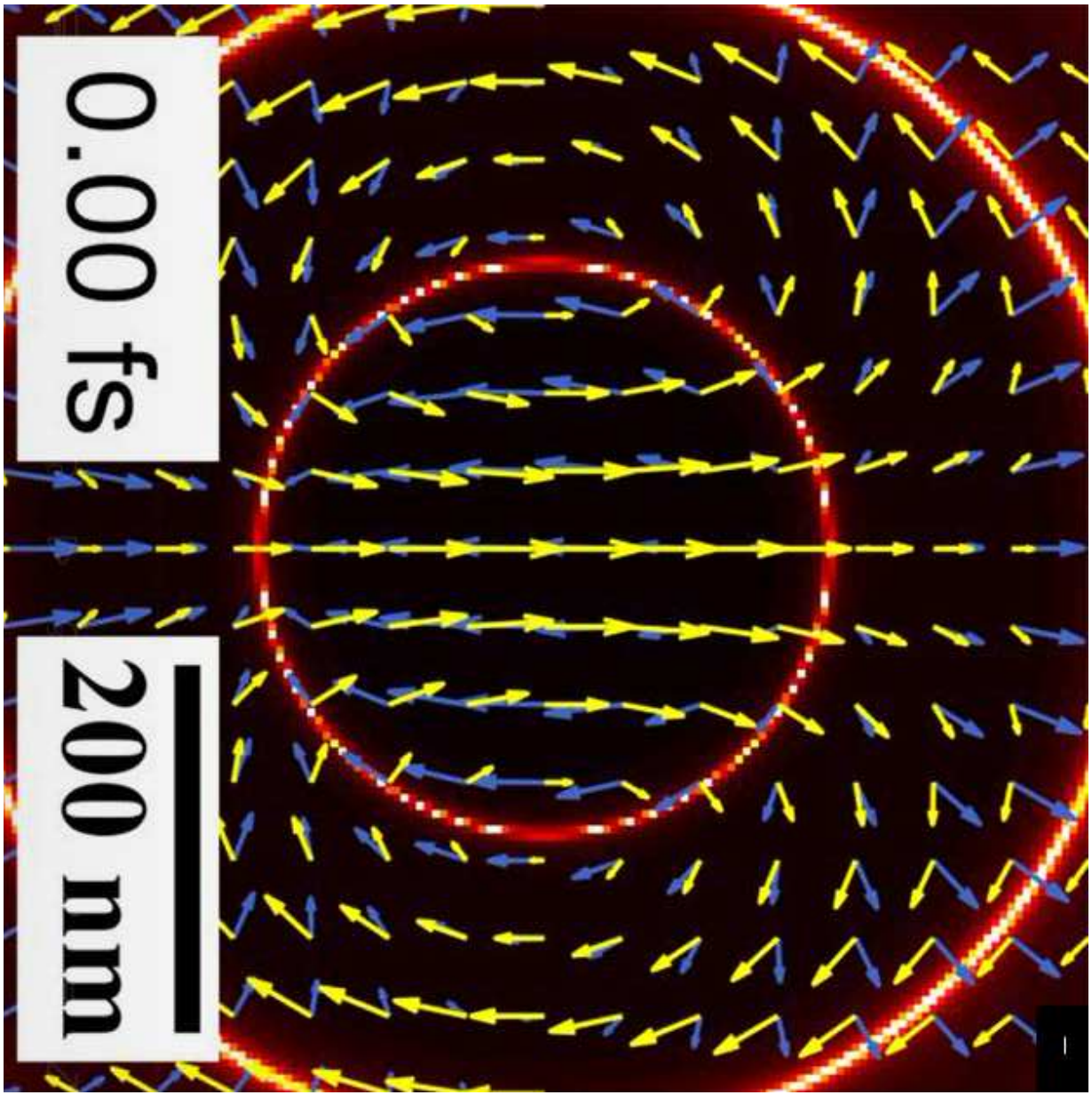

PLEASE CITE THIS ARTICLE AS DOI: 10.1063/5.0084482